Stress Interaction Behaviour in Alveolar Cortical Bone Fracture

*Noor Alia Md Zain[*1], Ruslizam Daud[2], Muhamad Safwan Muhamad Azmi[3], Nurul Huda Abdul Aziz[4], Siti Noor Fazliah Mohd Noor[5], Norie Allafi Ali Akeel[6]*

[1,4]Institute of Engineering Mathematics, Universiti Malaysia Perlis, Malaysia
[*]aliazain@unimap.edu.my

[2,3]Fracture and Damage Mechanics (FDM), Universiti Malaysia Perlis, Malaysia

[5]Advanced Medical and Dental Institute, Universiti Sains Malaysia, Malaysia

[6]Faculty of Engineering, Sohar University, Oman

ABSTRACT

Improving the mechanical integrity of the dental implantation through optimal stress distribution between the implant and the surrounding bone has reduced the risk of bone injury and implant loosening risk. Inversely, the clinical failure of implantation will result in the formation of microcracks in the alveolar bone. The uncertainty of stress interaction intensity between microcracks has been an unsolved issue regarding the load transfer between the implant and alveolar bone. This study investigates the magnitude of stress shielding and stress amplification to explain the behaviour of double edge (DE) microcracks that are identically formed due to various stability conditions of implantation under occlusal loading. A series of finite element modelling have been conducted to simulate the stress shielding and stress amplification behaviour based on the displacement extrapolation method (DEM) and contour integral analysis. The occlusal loading schemes are translated into Mode I, Mode II and Mixed-mode loading. The presented DE models have demonstrated the transition behaviour of DE parallel microcracks into a single edge (SE) crack basic behaviour, where the crack unification limit (CUL) and crack interaction limit (CIL) are identified at lower and a higher rates of a/W. The occlusal loading has shown significant influence on the intensity of stress shielding and stress amplification behaviour in a form of DE-SE microcracks interaction for Mode I and Mixed-mode occlusal loading.

Keywords: *Stress Shielding; Stress Amplification; Finite Element; Bone-Implant Interaction*

Introduction

The anchoring stability of dental implantation will lead to better osseointegration and bone healing. The initial mechanical engagement between the implant and the surrounding bone towards the implant provided primary implant stability, which is commonly viewed as an indicator of good osseointegration [1]. Primary implant stability was gradually replaced by secondary implant stability, which was obtained through new bone creation, bone apposition, and implant-bone interface remodelling [2]. However, the primary stability stage is affected by the quality and density of bone, the properties of the dental implant surface and the surgical approach. In most cases, dental implant failure was caused by an unstable dental implant fixation. Metal implant failure can be triggered by a mixture of factors, including the metal's material qualities (e.g., high stiffness, high corrosion rate, and toxicity) or the bone's exposure to infected metal implants (i.e., infection) [3]. In addition, the implantation loading method resulted in complicated stress shielding and stress concentration in most cases. Numerous factors contribute to the success of dental implantations. The stress distribution at the bone-implant interface is one of the critical issues. Some compressive pressures are required at the interface to induce osteointegration. However, the excessive stress will result in bone resorption which also caused implant failure [4].

Stiff implants alter the distribution of forces in the attached bone. The implant may act as a load shield, concentrating forces in different areas of the surrounding bones (e.g., at the site of fixation hardware screws). Assume that stress-shielding minimises the previously seen load in the vicinity of the implant. In that instance, those areas may remodel in response, decreasing total bone tissue volume and density (osteopenia). This insulated bone will shrink in size (external remodelling) and become more porous (internal remodelling), weakening it. Furthermore, if stress is focused on parts of the bone that have not previously been subjected to significant loads, the bone can be damaged, resulting in a fracture. This happens when implants constantly transmit too much load to previously under fewer strain regions. In the mechanism of implant-bone load transfer, various studies highlighted the load transfer is mostly transferred to the cortical bone rather than trabecular bone [5]–[7] In cortical bone fracture, the magnitude and direction of the force acting on the implant and the contour shape of the implant are critical factors along with the bone-implant contact and bone-implant interface [5] Indeed, the load transfer due to applied occlusal force is complicated due to loading morphology in the cortical and trabecular bone along with the bone-implant interface. Therefore, this study was to investigate the cortical bone fracture behaviour based on the

cortical bone fracture evidence at the apical region of an implant-bone system subjected to an occlusal loading scheme. The research hypothesis was that the microcracks formation initiated by various acting forces and load transfer increases or decreases the stress interaction intensity, thus increasing the failure probability through stress shielding or stress amplification. Numerous variables affect implant stability at the bone-implant interface, including the kind of loading, surface structure, the quantity of surrounding bone, material qualities, and implant design [8]. Consequently, the focus of this study was to examine the effects of stress shielding and stress amplification on the stability of bone-implant contact. The structure of the implants, the distribution of the interface stress, and the combination mode of the interface are the primary variables contributing to the stability of implants. Crucially, the load should be controlled to avoid surpassing the implant's physiological tolerance, as overloading might result in bone resorption or fatigue failure. Underloading, on the other hand, may result in disuse atrophy and consequent bone loss [9].

Failures of dental implant placement contribute to fracture and failure caused by interacting cracks. Multiple stress concentration features, including notches, holes, corners, and bends, are incorporated into the design of biomechanical structures and components, which affect the implantation procedures. Multiple stress riser points exist at each point of stress concentration where the field of stress is most concentrated. Under multiple modes of loading and environmental effect, the interaction between concentrated stress and multiple stress risers tends to form multiple cracks in various orientations before the cracks propagate along different paths to coalescence, overlapping, branching, and finally fracture in a brittle manner. Previous studies have shown that there have been numerous disastrous failures because of crack interaction brought from the multiple stress riser point [10]–[12]. Thus, the cases from past studies demonstrated the significance and importance of crack interaction investigation to prevent implantation failures. In this study, the established approach is addressed to the equality of two cracks to single crack standards in the fitness of service (FFS) code based on the crack interaction limit (CIL) aspects and crack unification limit (CUL) between the double parallel edge cracks in the developed finite element model. Common characteristics of the formation of two offset cracks include a sequence in which approaching crack tips frequently deviate to some degree from their former courses and propagate beyond one another before turning towards the opposite crack and merging with it. The interaction zone and coalescence conditions derived by Kitagawa et al. considered the changes in the stress intensity variables caused by the formation of a nearby fracture [13]-[14]. The SIF value of the nearest tips may dramatically increase when two cracks with a close lateral gap. Consequently, the stress interaction at the interacting crack points may be amplified, have no effect, or be reduced due to the shielding effect when compared to that of an isolated crack. Thus, the variation and the intersection of the stress interaction between the two parallel crack is the CUL

and CIL points, where the behaviour of two parallel cracks are merged into a single crack behaviour.

Materials and Models

Based on the transformation of clinical fracture [6], as shown in Figure 1 and alveolar bone fracture studies. The geometry of bone is investigated infinite continuum body and the interaction of microcracks is based on the Kachanov model. The geometry of the double edge (DE) cracks in the finite body element is constructed by nine models with nine different crack-to-width (*a/W*) ratios for Mode I, Mode II, and Mixed Mode analysis. It is generated in this section by the transition from the physical model of the actual fracture [15] from the mandibular clinical cases to the continuum body. For the double edge microcrack with the existence of the lower crack tip, c_1, upper crack tip, c_2, lower crack tip, ct_1 and upper crack tip, ct_2 in the human mandibular bone, a two-dimensional (2D) geometrical design of the finite element (FE) model is constructed, which was generated using ANSYS Parametric Design Language (APDL) macro coding based on the Kachanov theory of interaction. The interaction behaviour between the two microcracks is examined by the categories of the weak and strong interaction (shielding and amplification conditions) subjected to FFS geometrical design for the 2D continuum body. A similar method has been conducted in recent literature done by Imène Hebbar et. al [16].

There are four parameters design the geometry of the alveolar bone: the width of the continuum model *W* (1 *mm*), the upper crack length, a_1 ($0.125\,mm \leq a \leq 0.5\,mm$), the lower crack length a_2 (0.125 *mm*), and the crack interval,*b* ($0.1\,mm \leq a \leq 0.3\,mm$) between the double edge crack, *b*. For the alveolar cancellous bone tissue in the finite element model, the material properties are as follows: Young Modulus (1 GPa), Poisson's Ratio (0.25), and Occlusal Pressure (11 Pa). Three different loading modes—Mode I, Mode II, and Mixed-mode have been used.
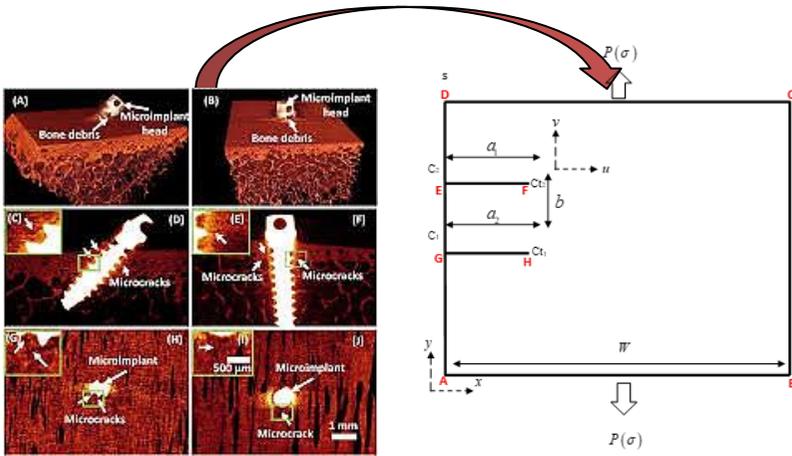
Figure 1: Transformation of the clinical fracture [15] to finite continuum body

Research design and material properties

A simplified representation of the bone's linear elastic material property based on a prior study [15]. The transformation from the clinical fracture to the finite continuum body generated using computational approaches is illustrated in Figure 1. Under 11 N tensile loading of occlusal force [7], both single edge and multiple edge cracks are modeled in the finite body [6], resulting in a force concentration around the crack points. The numerical model's dimension of is built to reflect the stress transfer between the dental implant and the microcracks behaviour found in several implant thread locations (cervical, central, and apical), a manner similar to that used in earlier studies[18]. The finite element's boundary condition is kept constant at the bottom line of the finite element model and the bottom left corner node The structural analysis performed with APDL is based on the data from finite element FE modelling. Table 1 shows the geometrical model points (A–H) of the implant geometry specified in (x, y) coordinate system.

In this study, crack interaction is limited to non-propagating cracks, where the shielding effect plays a significant role in promoting fracture and failure. The model included the relative position of two parallel edge cracks when the crack interval and crack-to-width ratio are varied. In addition, the stress intensity factor (SIF) and elastic crack interaction factor values are compared to the related FFS rules and numerical data from the literature. The SIF is limited to linear elastic problems involving a homogenous, isotropic material near the crack site.

The SIF is calculated using a quadratic isoparametric FE to create a single element at the fracture tip. A quarter-point singular element or eight-

127

node collapsed quadrilateral element invented by Henshell and Shaw [19] is employed in situations where it offers specific advantages over the other quarter-point element in terms of time, meshing, and re-mesh. The singularity is obtained by relocating the mid-side node four points closer to the crack tip. To compute the SIF, we assumed rigid body motion and constant strain modes for the elements. Murakami [20] addressed the accuracy of this special element by enclosing the crack tip nodal point in several particular elements and demonstrating that the size, number, and compatibility of certain elements had a significant effect on accuracy.

Table 1: Coordinates of the implant geometry's specific points

|	x	y
A	0	0
B	W	0
C	W	W
D	0	W
E	0	
F	0 a	
G	0	0.25
H	0.5	0.25
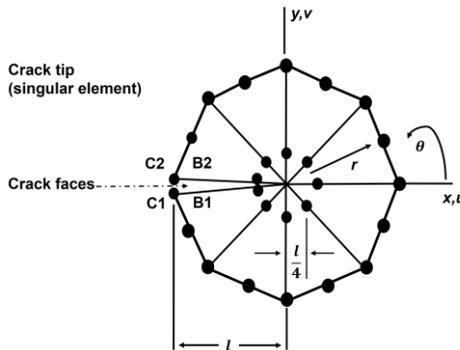
Figure 2: The quarter-point singular element introduced by Barsoum [21]

Figure 2 shows the Barsoum singularity element [21] that used to govern Equation (3) and Equation (4), known as the Displacement Extrapolation Method (DEM). The DEM is used to calculate the SIFs (K_I and K_{II}) in a mixed-mode problem based on the displacement of the crack side nodes of the singular element.

$$K_I = \frac{2\mu}{\kappa+1}\sqrt{\frac{\pi}{2l}}\Big[\big(4V_{B2}-V_{C2}\big)-\big(4V_{B1}-V_{C1}\big)\Big] \qquad (1)$$

$$K_{II} = \frac{2\mu}{\kappa+1}\sqrt{\frac{\pi}{2l}}\Big[\big(4V_{B2}-U_{C2}\big)-\big(4V_{B1}-U_{C1}\big)\Big] \qquad (2)$$

where μ is the shear modulus equals to $\frac{E}{2(1+\nu)}$, E is the Young's modulus, ν is the Poisson's ratio, $\kappa=(3-4\nu)$ for plane strain while $\kappa=\frac{(3-4\nu)}{1+\nu}$ for plane stress, U is for sliding displacement and V is for opening displacement located at the crack tip of the model. The DEM method has been widely used in FE analysis due to its simplicity, and the method reduce storage space and calculation time. However, this method has limitations when the SIF accuracy is highly dependent on the grid element refinement, which is supported by Liao in recent studies [22] Nevertheless, according to Brocks et al. [23], the DEM method is unreliable in modern research because it relies on the singularity element, which yields significantly more precise results. The CINT method, on the other hand, produces consistent and accurate results even for coarse meshes and does not require the arrangement of singularity elements. Unfortunately, the CINT is unable to accurately determine the crack tip opening displacement (CTOD) or stresses at the crack tip for stationary cracks [23]. This study uses both DEM and CINT to determine the most accurate and reliable strategy for the established finite element model.
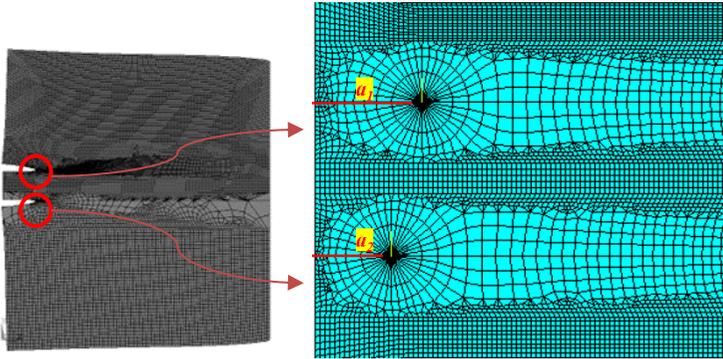

Figure 3: Geometrical model and meshing scheme

The mesh that encloses the interacting fractures is separated into global and local mesh zones. Both zones are meshed using the eight-node isoparametric quadrilateral element that serves as the foundation for the two-dimensional plate element, as depicted in

Figure 3. PLANE 42, an ANSYS solid element, was employed with plane strain assumption. This assumption was necessary due to the enormous number of elements needed to solve rapid stress changes in precise detail. The element size is determined by their distance from the crack tip surface, as shown in

Figure 3. The geometry was discretized using two-dimensional isoparametric elements with eight nodes, quadratic shape functions, and plane strain behaviour. Utilizing degenerated components of the same type, the crack tip has been provided with greater precision. In particular, the quarter-point position is occupied by the mid-side node of the two sides closest to the crack tip node. This element type is also known as the quarter-point element.

Sensitivity analysis and theoretical validation

Convergence meshing is used to choose the optimal meshing scheme around the crack tip at the local concentration keypoint, resulting in precise numerical results for the SIFs. The optimal value for the meshing element is determined by the number of wedges surrounding the crack tip element (NTHET). NTHET is varied between 6 and 24, and the sensitivity analysis of the simulation results is based on converged element numbers, which improve model accuracy.
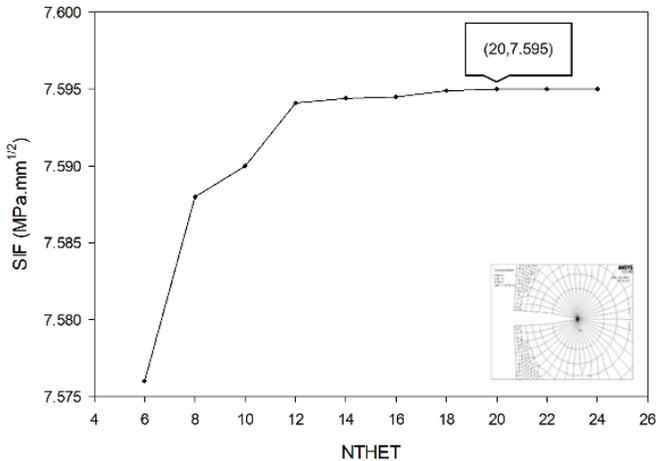

Figure 4: Meshing scheme sensitivity analysis based on the NTHET values

Figure 4 illustrates the variance in the meshing strategy for the optimum values based on the NTHET values. As can be observed, the SIF value increases with increasing NTHET values until it hits a plateau state at NTHET = 20, indicating the meshing scheme's optimal value. Thus, the number of

wedge elements and meshing areas adopted for this research will be implemented as depicted in

Figure 3. SIF is limited to linear elastic fracture mechanics (LEFM) behaviour in a homogenous, isotropic material surrounding the crack tip zone. A few analytical SIF from previous researchers by Brown & Srawley [24], Tada [25], and Gross & Brown [26] have offered a recommended reference based on analytical data from previous investigations.

The large discrepancy in the SIF value between the numerical and analytical data is illustrated in Figure 5. As can be seen, the numbers for the displacement extrapolation method (DEM) and contour integral (CINT) method, are nearly identical, except for a minor percentage difference for the DEM and CINT. Thus, the numerical model built in this study is deemed appropriate to analyse the stress behaviour of double microcracks under various crack length to width ratio situations. The CINT approach is more precise than the DEM method. Thus, the CINT technique is employed in this analysis to compute SIFs.
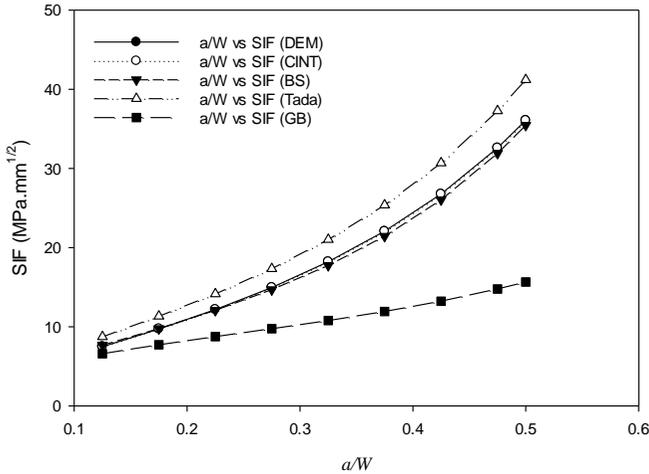
Figure 5: Comparison of the numerical stress intensity factor with the analytical data

Numerical result and discussion

The relationship between a parallel microcrack (upper crack tip surface) and a primary crack (lower crack tip surface) under Mode I, Mode II, and Mixed-mode loadings are considered. The SIF is limited to LEFM behaviour in the presence of a homogenous, isotropic material surrounding the crack tip zone.

Table 2 shows the percentage error for the numerical model of double edge microcracks. According to the acquired results, the percentage error for

all SIF readings was less than 0.03 percent, with an average error of 0.02 percent.

Table 2: Percentage error of the developed numerical model measured from the previous analytical data

a/W	SIF (CINT)	SIF(BS)	% SIF(BS)
0.125	7.4731	7.6644	0.026
0.175	9.7137	9.7644	0.005
0.225	12.1630	12.0630	0.008
0.275	14.9530	14.6736	0.019
0.325	18.2020	17.7343	0.026
0.375	22.0770	21.4372	0.029
0.425	26.7760	26.0473	0.027
0.475	32.6130	31.9166	0.021
0.500	36.0950	35.4601	0.018
Average error (%)			0.020

For validation reasons, the findings for all numerical readings are collected from a single edge crack numerical model and compared to the preceding analytical model (Brown & Srawley) [26]. The SIF of the analytical model used is derived from the following equation:

$$K_{BS} = \sigma\sqrt{\pi a}\left(1.12 - 0.23\left(\frac{a}{W}\right) + 10.6\left(\frac{a}{W}\right)^2 - 21.7\left(\frac{a}{W}\right)^3 + 30.4\left(\frac{a}{W}\right)^4\right) \quad (3)$$

$$K_{BS} = \sigma\sqrt{\pi a}\left(f_{1,BS}\right) \quad (4)$$

where σ is the pressure given to the model and $f_{1,BS}$ is the shape correction factor for the single edge crack for the FE model. The results indicate that the proposed numerical model is accurate and validated for application to the model of double edge cracks.

The SIFs are shown for the CINT to illustrate the effect of the microcrack crack length to width ratio (a/W) and crack interval, b on the primary microcrack interaction. A similar finding was found in recent studies where the SIF varies along the a/W and b magnitude [27]-[28]. Numerical findings are presented for three loading modes: Mode I, Mode II, and Mixed-mode loading. The SIF values in Table 3 are for the upper and lower crack tips, respectively. The Ct_{ref} is extracted from the single edge crack model and compared to the double edge crack model to determine the amplification and shielding behaviour of the FE model. The upper crack tip has a varied crack length between $0.125 \leq \frac{a}{W} \leq 0.5$ length and the stress interaction condition

behaviour between the two parallel crack tips. Due to the presence of a microcrack, the stress intensity factor at the tip of the main crack may be enhanced ($\frac{SIF_{ct1}}{SIF_{ct\_ref}}, > 1$, amplification) or suppressed ($\frac{SIF_{ct1}}{SIF_{ct\_ref}} < 1$, shielding).

The transition from stress shielding to stress amplification happens particularly at the crack intervals $b = 0.1$ mm and $b = 0.15$ mm for Mode I loading. The interaction between the two crack tips exhibits the same amplification behaviour when the crack interval is greater than 0.15 mm. The transition between the two stress behaviours occurs most significantly at $a/W = 0.125$ mm, 0.475 mm, and 0.5 mm, respectively. Interestingly, at $\frac{SIF_{ct1}}{SIF_{ct\_ref}} = 1$, two parallel edge cracks without interaction occurred, which is equivalent to a single independent crack. This stage allows for the determination of the crack interaction limit (CIL). This occurs as the stress behaviour transitions between the shielding and amplification phases. However, there is no transition between the stress behaviour phases for Mode II loading conditions. For all crack length and crack interval configurations, the two parallel edge cracks display solely the stress amplification stress behaviour. According to the numerical results in Mode I, the two parallel edge microcrack interactions exhibit two distinct behaviours (stress shielding and stress amplification).

Table 3: The stress condition in the double edge crack for Mode I loading condition

a/W	B = 0.1				
	SIF, ct$_1$	SIF, ct$_2$	SIF, ct$_{ref}$	SIF, ct$_1$ /ct$_{ref}$	Stress condition
0.125	6.623	5.428	7.4731	0.886	Shielding
0.175	10.680	2.229	9.7137	1.100	Amplification
0.225	13.836	0.118	12.163	1.138	Amplification
0.275	16.883	1.363	14.953	1.129	Amplification
0.325	20.109	2.102	18.202	1.105	Amplification
0.375	23.471	0.610	22.077	1.063	Amplification
0.425	26.922	0.730	26.776	1.005	Amplification
0.475	30.374	0.809	32.613	0.931	Shielding
0.5	32.054	0.844	36.095	0.888	Shielding
	B = 0.15				
0.125	7.050	5.712	7.4731	0.943	Shielding
0.175	10.778	3.521	9.7137	1.110	Amplification
0.225	14.222	2.577	12.163	1.169	Amplification
0.275	17.584	1.290	14.953	1.176	Amplification
0.325	21.095	0.571	18.202	1.159	Amplification
0.375	24.756	0.252	22.077	1.121	Amplification

0.425	28.548	0.165	26.776	1.066	Amplification
0.475	32.393	0.210	32.613	0.993	Shielding
0.5	34.289	0.262	36.095	0.950	Shielding
			$B = 0.2$		
0.125	7.559	5.969	7.4731	1.011	Amplification
0.175	11.215	5.463	9.7137	1.155	Amplification
0.225	14.934	3.702	12.163	1.228	Amplification
0.275	18.711	2.220	14.953	1.251	Amplification
0.325	22.675	1.178	18.202	1.246	Amplification
0.375	26.829	0.746	22.077	1.215	Amplification
0.425	31.172	0.469	26.776	1.164	Amplification
0.475	35.647	0.393	32.613	1.093	Amplification
0.5	37.891	0.407	36.095	1.050	Amplification
			$B = 0.25$		
0.125	8.153	6.803	7.4731	1.091	Amplification
0.175	11.998	5.578	9.7137	1.605	Amplification
0.225	16.124	4.111	12.163	2.158	Amplification
0.275	20.499	2.699	14.953	2.743	Amplification
0.325	25.144	1.540	18.202	3.365	Amplification
0.375	30.090	0.690	22.077	4.026	Amplification
0.425	35.326	0.117	26.776	4.727	Amplification
0.475	40.796	0.237	32.613	5.459	Amplification
0.5	43.586	0.350	36.095	5.832	Amplification
			$B = 0.3$		
0.125	9.267	6.479	7.4731	1.240	Amplification
0.175	13.544	6.572	9.7137	1.812	Amplification
0.225	18.352	5.323	12.163	2.456	Amplification
0.275	23.627	4.012	14.953	3.162	Amplification
0.325	29.393	2.821	18.202	3.933	Amplification
0.375	35.597	1.855	22.077	4.763	Amplification
0.425	42.254	1.140	26.776	5.654	Amplification
0.475	49.345	0.917	32.613	6.603	Amplification
0.5	53.021	0.794	36.095	7.095	Amplification

Table 4: The stress condition in the double edge crack for Mode II loading condition

| | | | | $B = 0.1$ | |
a/W	SIF, ct_1	SIF, ct_2	SIF, ct_{ref}	SIF, ct_1/ct_{ref}	Stress condition
0.125	0.811	0.437	7.77E-03	1.04E+02	Amplification
0.175	1.050	0.174	2.85E-07	3.68E+06	Amplification
0.225	1.175	0.067	5.86E-07	2.01E+06	Amplification

0.275	1.292	0.033	3.56E-07	3.63E+06	Amplification
0.325	1.425	0.024	7.13E-07	2.00E+06	Amplification
0.375	1.581	0.022	9.08E-08	1.74E+07	Amplification
0.425	1.765	0.022	8.06E-08	2.19E+07	Amplification
0.475	1.991	0.022	5.59E-07	3.56E+06	Amplification
0.5	2.125	0.023	7.9E-07	2.69E+06	Amplification
$B = 0.15$					
0.125	0.638	0.408	7.77E-03	8.21E+01	Amplification
0.175	0.807	0.293	2.85E-07	2.83E+06	Amplification
0.225	0.916	0.213	5.86E-07	1.56E+06	Amplification
0.275	1.005	0.173	3.56E-07	2.83E+06	Amplification
0.325	1.002	0.227	7.13E-07	1.41E+06	Amplification
0.375	1.205	0.146	9.08E-08	1.33E+07	Amplification
0.425	1.437	0.088	8.06E-08	1.78E+07	Amplification
0.475	1.490	0.138	5.59E-07	2.67E+06	Amplification
0.5	1.583	0.138	7.9E-07	2.01E+06	Amplification
$B = 0.2$					
0.125	0.463	0.435	7.77E-03	5.96E+01	Amplification
0.175	0.807	0.673	2.85E-07	2.83E+06	Amplification
0.225	0.689	0.361	5.86E-07	1.18E+06	Amplification
0.275	0.766	0.337	3.56E-07	2.15E+06	Amplification
0.325	0.838	0.321	7.13E-07	1.18E+06	Amplification
0.375	0.916	0.311	9.08E-08	1.01E+07	Amplification
0.425	1.004	0.305	8.06E-08	1.25E+07	Amplification
0.475	1.111	0.301	5.59E-07	1.99E+06	Amplification
0.5	1.173	0.300	7.9E-07	1.49E+06	Amplification
$B = 0.25$					
0.125	0.376	0.315	7.77E-03	4.84E+01	Amplification
0.175	0.451	0.299	2.85E-07	1.58E+06	Amplification
0.225	0.514	0.283	5.86E-07	8.78E+05	Amplification
0.275	0.569	0.270	3.56E-07	1.60E+06	Amplification
0.325	0.620	0.260	7.13E-07	8.69E+05	Amplification
0.375	0.672	0.253	9.08E-08	7.40E+06	Amplification
0.425	0.728	0.248	8.06E-08	9.04E+06	Amplification
0.475	0.794	0.245	5.59E-07	1.42E+06	Amplification
0.5	0.832	0.243	7.9E-07	1.05E+06	Amplification
$B = 0.3$					
0.125	0.139	0.600	7.77E-03	1.79E+01	Amplification
0.175	0.251	0.621	2.85E-07	8.79E+05	Amplification
0.225	0.344	0.580	5.86E-07	5.87E+05	Amplification
0.275	0.422	0.639	3.56E-07	1.19E+06	Amplification
0.325	0.490	0.643	7.13E-07	6.87E+05	Amplification
0.375	0.552	0.640	9.08E-08	6.08E+06	Amplification
0.425	0.610	0.636	8.06E-08	7.57E+06	Amplification

0.475	0.669	0.632	5.59E-07	1.20E+06	Amplification
0.5	0.700	0.630	7.9E-07	8.87E+05	Amplification

Table 5: The stress condition in the double edge crack for Mixed-mode loading condition

	$B = 0.1$				
a/W	SIF, ct_1	SIF, ct_2	SIF, ct_{ref}	SIF, ct_1 /ct_{ref}	Stress condition
0.125	9.403	7.587	7.7944	1.206	Amplification
0.175	5.699	13.368	10.288	0.554	Shielding
0.225	2.411	18.089	13.13	0.184	Shielding
0.275	0.795	22.706	16.373	0.049	Shielding
0.325	0.009	27.740	20.112	0.000	Shielding
0.375	0.418	33.438	24.501	0.017	Shielding
0.425	0.628	40.028	29.735	0.021	Shielding
0.475	0.728	47.894	36.207	0.020	Shielding
0.5	0.751	52.479	40.048	0.019	Shielding
	$B = 0.15$				
0.125	7.783	9.754	7.7944	0.999	Shielding
0.175	12.762	7.213	10.288	1.240	Amplification
0.225	17.584	4.536	13.13	1.339	Amplification
0.275	22.402	2.554	16.373	1.368	Amplification
0.325	27.561	1.297	20.112	1.370	Amplification
0.375	33.314	0.544	24.501	1.360	Amplification
0.425	39.909	0.110	29.735	1.342	Amplification
0.475	47.684	0.125	36.207	1.317	Amplification
0.5	52.169	0.191	40.048	1.303	Amplification
	$B = 0.2$				
0.125	8.158	10.020	7.7944	1.047	Amplification
0.175	12.779	8.223	10.288	1.242	Amplification
0.225	17.661	6.092	13.13	1.345	Amplification
0.275	22.739	4.182	16.373	1.389	Amplification
0.325	28.178	2.743	20.112	1.401	Amplification
0.375	34.181	1.760	24.501	1.395	Amplification
0.425	40.974	1.135	29.735	1.378	Amplification
0.475	47.684	0.125	36.207	1.317	Amplification
0.5	52.169	0.191	40.048	1.303	Amplification
	$B = 0.25$				
0.125	8.842	10.267	7.7944	1.134	Amplification
0.175	13.445	8.914	10.288	1.307	Amplification
0.225	18.559	7.214	13.13	1.414	Amplification
0.275	24.055	5.513	16.373	1.469	Amplification

0.325	30.005	4.068	20.112	1.492	Amplification
0.375	36.565	2.974	24.501	1.492	Amplification
0.425	43.887	2.221	29.735	1.476	Amplification
0.475	52.236	1.754	36.207	1.443	Amplification
0.5	56.917	1.608	40.048	1.421	Amplification
B = 0.3					
0.125	11.4540	9.9379	7.7944	1.470	Amplification
0.175	14.8486	9.4554	10.288	1.443	Amplification
0.225	20.5376	8.0727	13.13	1.564	Amplification
0.275	26.8449	6.5839	16.373	1.640	Amplification
0.325	33.7886	5.2043	20.112	1.680	Amplification
0.375	41.4629	4.0727	24.501	1.692	Amplification
0.425	49.9649	3.2374	29.735	1.680	Amplification
0.475	59.5026	2.6904	36.207	1.643	Amplification
0.5	64.7572	2.5145	40.048	1.617	Amplification

For Mixed-mode loading situations, the stress behaviour demonstrates a discrete transition state between stress behaviour phases. At $b \geq 0.15$ mm, for instance, the stress interaction behavioural changes from a shielding phase to an amplification phase along the variation of a/W in the upper crack tip. At the same a/W crack length, the SIF between the upper and lower crack tips is nearly identical. For the combination of tensile and shear loading conditions, the stress concentration acted on both crack tips is equally balanced (Mixed-mode loading). In contrast to the SIF at solely tensile (Mode I) and shear (Mode II) loading directions, the SIF in the upper and lower crack tip have substantial variances at comparable a/W crack lengths. The relationship between the crack interval, b, and the crack length, a, also affects the interaction between two parallel edge cracks. For instance, if the distance between two equal cracks is less than the strength of the cracks, b/a there is a strong interaction between them. Secondly, the cracks exhibit a weak interaction when the distance between two parallel fractures exceeds the primary crack length which agrees with Kachanov's theory of interaction [29]-[31].

Figure 6 depicts the variation difference between the stress interaction behaviour of the amplification and shielding in Mode I and Mixed-mode loading schemes. At the closest crack interval between two parallel edge cracks, the Mode I interaction begins to exhibit shielding behaviour. As a/W increases, the stress interaction increases, and hence, stress amplification occurs. As the a/W length approached 0.5 mm, however, the stress interaction between the two crack tips diminished and the behaviour reverted to the shielding stress behaviour. In contrast, the mixed-mode situation exhibits a distinct transition where the stress interaction commences off as an amplification stress behaviour and decreases as the a/W grows.
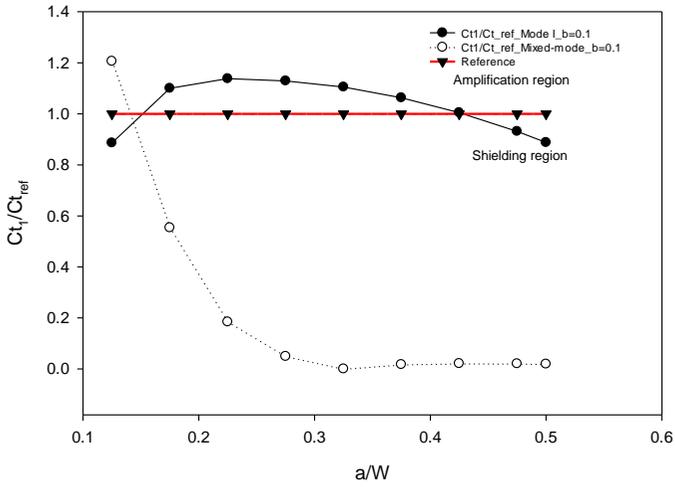
(a) $b = 0.1$ mm
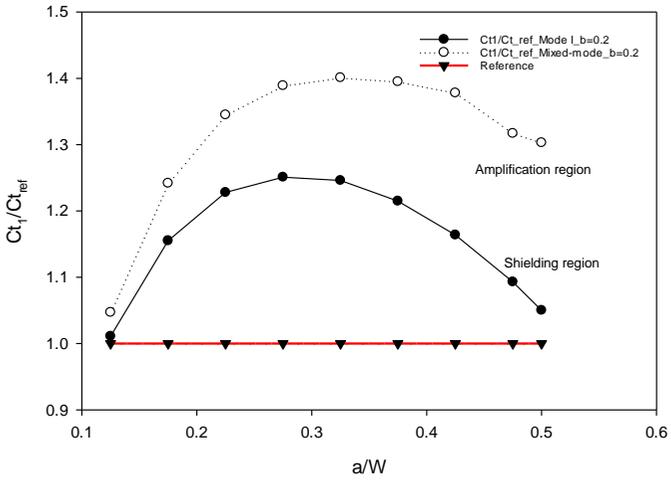
(b) $b = 0.2$ mm

(c) *b* = 0.3 mm
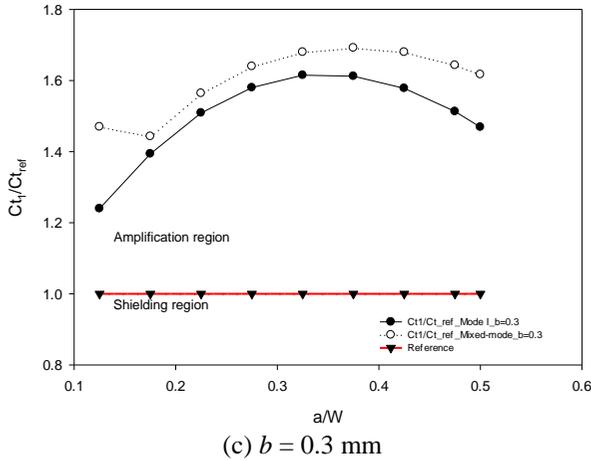
Figure 6: Variation of normalized interaction of the stress intensity factor

The difference in stress interaction behaviour is due to the effect of the difference between the purely tensile load in Mode I and the combination of tensile and shear loads in the Mixed-mode loading scheme on the SIF existing in both of the crack tips. When the two crack tips are close to each other, there is a strong interaction between the two crack tips. Thus, the loading direction in the continuum finite element model has a significant effect on the stress interaction between the two parallel edge cracks. As the two parallel crack tip surfaces grow apart from each other, the stress interaction variation for Mode I and Mixed-mode loading conditions is nearly identical. For both loading circumstances, the stress interaction between the two crack tips exhibits an amplification behaviour. Interestingly, as the *a/W* rises, the amplification behaviour increases as well. However, as *a/W* approaches 0.3 mm, there is a variability in the stress interaction behaviour. Thus, it can be seen that there is a significant reduction in the magnitude of the stress interaction between the two crack tips at the longer *a/W* lengths.

In general, when two cracks are parallel, the longer fracture will experience a greater SIF and may serve as a propagation crack site. In the parallel crack interaction, when the size of one of the cracks rises, its crack tip absorbs more stress while the stress on the other crack tip drops, hence amplifying the crack-tip of the longer crack. When the lengths of two cracks are identical, the stress or load at the crack points is also same. According to previous study, the maximum value of the lateral crack interval, *b*, required to produce coalescence is dependent on the crack length, *2a* [14] following:

$$h \leq 0.14(2a) \tag{5}$$

The *b/2a* ratio between the two parallel crack tips plays a crucial role in predicting the stress interaction behaviour between the two parallel crack tips, and the similar findings has been reported by previous research [30]. Thus, for the analysis of crack interaction in this study, the SIF for the closest tip of two parallel cracks in an infinitely elastic solid subjected to a tensile stress is utilised.

The numerical results presented in Table 3-**Error! Reference source n ot found.** also demonstrate the prediction pattern for all crack length to width ratios and crack intervals for Mode I and Mixed-mode loading conditions. Two conditions should be observed in this case. To commence, there is a distinct trend of stress shielding to stress amplification transition at the crack interval, *b* = 0.1 mm, under Mode I and Mixed-mode loading circumstances. Second, except for the Mixed-mode loading at the crack interval, *b* = 0.3 mm, the stress amplification dominated the stress behaviour of all crack interval length configurations. Concerning the present interacting shielding factor, which is relevant to the energy release rate, there are two situations of interaction that occur: crack unification limit (CUL) and crack interaction limit (CIL).

The variability in the stress shielding factor is illustrated in Figure 7, employing Brown & Srawley's reference analytical data [32]. A few interacting cracks can be seen. At the higher intersection point of *a/W*, the two parallel edge cracks with no interaction are equivalent to a single independent crack. This stage enables the determination of the crack interaction limit (CIL). Two cracks are merged into a single crack in the following occurrence, and a strong interaction occurs, revealing the crack unification limit (CUL). When parallel cracks come into contact, a weak interaction occurs, which explains the CUL exists in the lower intersection point of *a/W*.


(a)

(b)

(c)
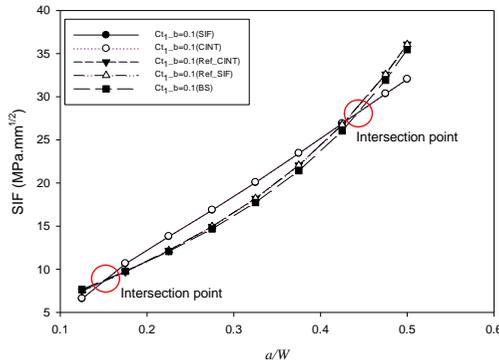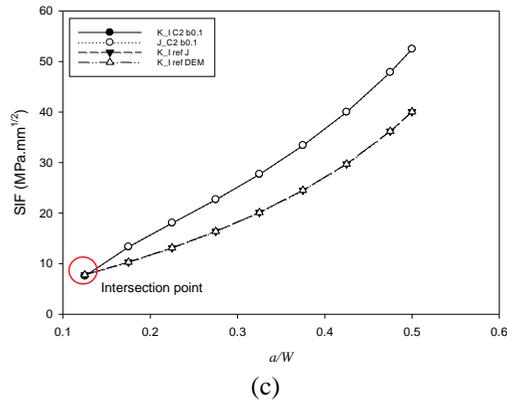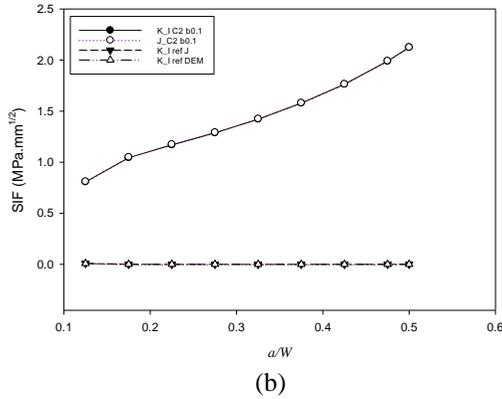
Figure 7: Variation of the stress shielding factor in (a) Mode I, (b) Mode II
and (c) Mixed-mode loading at crack interval *b*= 0.1 mm

Conclusion

This study found that the applied Mode I, Mode II and Mixed mode occlusal
loading exhibit different magnitudes of stress shielding and stress
amplification intensity. The transition of the DE microcracks to SE microcrack
is exist at the different magnitude of crack to width ratio, *a/W* and crack
interval, *b*. It was discovered that as the cracks' interval increases, the shielding
effect under Mode I occlusal stress transitions to the amplification effect. On
the other hand, when the fracture interval increases, Mixed-mode occlusal

loading displays the opposite behaviour as the size of the crack gap grows. Interestingly, it was discovered that the crack interval did not affect the stress shielding behaviour under Mode II loading conditions. Following that, we determined the crack interaction limit (CIL) and the crack unification limit (CUL). When b and a/W are increased or decreased, the SIF of Mode I and Mixed-mode loading conditions is deemed to be more significant than that of Mode II loading conditions. CIL and CUL are accurate representations of the numerical model that defines the merging cracks as a single crack.

Acknowledgement

References

[1] F. Javed and G. E. Romanos, "The role of primary stability for successful immediate loading of dental implants. A literature review," *Journal of Dentistry*, vol. 38, no. 8, pp. 612–620, Aug. 2010, doi: 10.1016/j.jdent.2010.05.013.

[2] S. Raghavendra *et al.*, "Early wound healing around endosseous implants: a review of the literature" *The Internatioanl Journal of Oral Maxillofac Implants*, vol. 20, no. 3, pp. 425-32, 2005.

[3] N. Shayesteh Moghaddam *et al.*, "Metals for bone implants: safety, design, and efficacy," *Biomanufacturing Reviews*, vol. 1, no. 1, 2016, doi: 10.1007/s40898-016-0001-2.

[4] P. Dhatrak, U. Shirsat, S. Sumanth, and V. Deshmukh, "Finite Element Analysis and Experimental Investigations on Stress Distribution of Dental Implants around Implant-Bone Interface," *Materials Today Proceedings*, vol. 5, no. 2, Part 1, pp. 5641–5648, 2018, doi: https://doi.org/10.1016/j.matpr.2017.12.157.

[5] S. Faegh and S. Müftü, "Load transfer along the bone–dental implant interface," *Journal of Biomechanics*, vol. 43, no. 9, pp. 1761–1770, 2010.

[6] P. Dhatrak, U. Shirsat, S. Sumanth, and V. Deshmukh, "Finite Element Analysis and Experimental Investigations on Stress Distribution of Dental Implants around Implant-Bone Interface," *Materials Today Proceedings*, vol. 5, no. 2, Part 1, pp. 5641–5648, 2018, doi: https://doi.org/10.1016/j.matpr.2017.12.157.

[7] E. Pérez-Pevida *et al.*, "Biomechanical Consequences of the Elastic Properties of Dental Implant Alloys on the Supporting Bone: Finite

Element Analysis," *Biomed Research International*, vol. 2016, pp. 1–9, 2016, doi: 10.1155/2016/1850401.

[8] N. Djebbar, A. Bachiri, and B. Boutabout, "Comparison of Stress Distribution in Surrounding Bone during Insertion of Dental Implants on Four Implant Threads under the Effect of an Impact: A Finite Element Study," in *Journal of Biomimetics, Biomaterials and Biomedical Engineering*, 2022, vol. 54, pp. 89–101.

[9] S. A. Hosseini-Faradonbeh and H. R. Katoozian, "Biomechanical evaluations of the long-term stability of dental implant using finite element modeling method: a systematic review," *The Journal of Advanced Prosthodontics*, vol. 14, no. 3, pp. 182, 2022.

[10] T. Davis, D. Healy, A. Bubeck, and R. Walker, "Stress concentrations around voids in three dimensions: The roots of failure," *Journal of Structural Geology*, vol. 102, pp. 193–207, 2017.

[11] D. Langer, S. Hassanien, and J. Woo, "Semi-Quantitative Reliability-Based Ranking Method for Assessment of Pipeline Dents With Stress Risers," in *International Pipeline Conference*, 2018, vol. 51876, p. V002T07A003.

[12] R. Picelli, S. Townsend, C. Brampton, J. Norato, and H. A. Kim, "Stress-based shape and stopology optimization with the level set method," *Computer Methods in Applied Mechanics and Engineerings*, vol. 329, pp. 1–23, 2018.

[13] H. Kitagawa, T. Fujita, and K. Miyazawa, *Small randomly distributed cracks in corrosion fatigue*. ASTM International, 1978.

[14] Y. Wang, J. D. Atkinson, R. Akid, and R. N. Parkins, "Crack interaction, coalescence and mixed mode fracture mechanics," *Fatigue & Fracture of Engineering Materials and Structures*, vol. 19, no. 1, pp. 51-63, 1996.

[15] H. T. Lakshmikantha, N. K. Ravichandran, M. Jeon, J. Kim, and H.-S. Park, "3-Dimensional characterization of cortical bone microdamage following placement of orthodontic microimplants using Optical Coherence Tomography," *Scietific Reports*, vol. 9, no. 1, pp. 1–13, 2019.

[16] I. Hebbar and A. Boulenouar, "Numerical and analytical study of the stress intensity factor in a mixed mode of isotropic fracture with a functionally graduated material," *International Journal on Interactive Design and Manufacturing (IJIDeM)*, pp. 1–7, 2022.

[17] Y. Ye, P. Di, S. Jia, and Y. Lin, "Occlusal force and its distribution in the position of maximum intercuspation in individual normal occlusion: a cross-sectional study," *Zhonghua Kou Qiang Yi Xue Za Zhi*, vol. 50, no. 9, pp. 536–539, 2015.

[18] A. Boulenouar, N. Benseddiq, and M. Mazari, "Two-dimensional numerical estimation of stress intensity factors and crack propagation in linear elastic analysis," *Engineering, Technology & Applied Science Research*, vol. 3, no. 5, pp. 506–510, 2013.

[19] N. Sakakibara, "Finite Element Method in Fracture Mechanics," *The University of Texas at Austin*, 2008.

[20] Y. Nadot, "Fatigue from Defect: Influence of Size, Type, Position, Morphology and Loading," *International Journal of Fatigue*, vol. 154, pp. 106531, 2022, doi: https://doi.org/10.1016/j.ijfatigue.2021.106531.

[21] H. Kim, W. G. Buttlar, and K. F. Chou, "Mesh-Independent Fracture Modeling for Overlay Pavement System under Heavy Aircraft Gear Loadings," *Journal of Transportation Engineering*, vol. 136, no. 4, pp. 370–378, Apr. 2010, doi: 10.1061/(ASCE)TE.1943-5436.0000101.

[22] M. Liao and P. Zhang, "An improved approach for computation of stress intensity factors using the finite element method," *Theoretical and Applied Fracture Mechanics*, vol. 101, pp. 185–190, 2019, doi: https://doi.org/10.1016/j.tafmec.2019.02.019.

[23] W. Brocks, A. Cornec, and I. Scheider, "Computational Aspects of Nonlinear Fracture Mechanics," in *Comprehensive Structural Integrity*, vol. 35, no. 24, pp. 127–209, 2003, doi: 10.1016/B0-08-043749-4/03102-5.

[24] G. E. Blandford, A. R. Ingraffea, and J. A. Liggett, "Two-dimensional stress intensity factor computations using the boundary element method," *International Journal for Numerical Methods in Engineering*, vol. 17, no. 3, pp. 387–404, 1981.

[25] H. Tada, P. C. Paris, and G. R. Irwin, "The stress analysis of cracks," *Handbook, Del Research Corporation*, vol. 34, p. 635, 1973.

[26] H. Tada, P. C. Paris, and G. R. Irwin, "The stress analysis of cracks," *Handbook, Del Research Corporation*, vol. 34, 1973.

[27] H. Wang, J. Huang, Z. Zhu, L. Zhou, R. Liu, and Y. Jiang, "A complex analysis of stress intensity factors for two asymmetric and unequal collinear cracks in rocks subjected to compressive and shear loads," *Theoretical and Applied Fracture Mechanics*, vol. 118, pp. 103258, 2022.

[28] A. Tanwar, R. Singh, S. Das, and H. Altenbach, "Interaction among offset parallel cracks in an orthotropic plane under thermo-mechanical loading," *ZAMM - Journal of Applied Mathematics and Mechanics*, vol. 102, no. 7, pp. e202100593, 2022, doi: 10.1002/zamm.202100593.

[29] M. Kachanov, E. L. E. Montagut, and J. P. Laures, "Mechanics of crack—microcrack interactions," *Mechanics of Materials*, vol. 10, no. 1–2, pp. 59–71, 1990.

[30] M. Kachanov, "Elastic Solids with Many Cracks and Related Problems," in *Advances in Applied Mechanics*, vol. 30, pp. 259–445, 1993, doi: 10.1016/S0065-2156(08)70176-5.

[31] B.-W. Xu, S. Ye, M. Li, H.-P. Zhao, and X.-Q. Feng, "Deep learning method for predicting the strengths of microcracked brittle materials," *Engineering Fracture Mechanics*, vol. 271, pp. 108600, 2022, doi: 10.1016/j.engfracmech.2022.108600.

[32] H. Tada, P. Paris, and G. Irwin, "The analysis of cracks handbook," *New York: ASME Press*, vol. 2, pp. 1, 2000.